Towards Arbitrary-scale Histopathology Image Super-resolution: An Efficient Dual-branch Framework based on Implicit Self-texture Enhancement

Linhao Qu[*1], Minghong Duan[*1], Zhiwei Yang[1,2], Manning Wang[✉1], Zhijian Song[✉1]

[1] Digital Medical Research Center, School of Basic Medical Science, Fudan University, Shanghai Key Lab of Medical Image Computing and Computer Assisted Intervention, Shanghai 200032, China, {mnwang, zjsong}@fudan.edu.cn
[2] Academy for Engineering & Technology, Fudan University, Shanghai 200433, China

Abstract. Existing super-resolution models for pathology images can only work in fixed integer magnifications and have limited performance. Though implicit neural network-based methods have shown promising results in arbitrary-scale super-resolution of natural images, it is not effective to directly apply them in pathology images, because pathology images have special fine-grained image textures different from natural images. To address this challenge, we propose a dual-branch framework with an efficient self-texture enhancement mechanism for arbitrary-scale super-resolution of pathology images. Extensive experiments on two public datasets show that our method outperforms both existing fixed-scale and arbitrary-scale algorithms. To the best of our knowledge, this is the first work to achieve arbitrary-scale super-resolution in the field of pathology images. Codes will be available.

Keywords: Super resolution · Histopathology image · Implicit neural network

1 Introduction

High-resolution pathology Whole Slide Images (WSIs) contain rich cellular morphology and pathological patterns, which are the basis for a series of automated pathology image analysis tasks [18,6,24,23]. However, the acquisition and use of high-quality WSIs remain limited in the daily clinical workflow [9]. On one hand, high-resolution WSIs need to be acquired by high magnification scanners [23], which are expensive and time-consuming to use. On the other hand, high-resolution WSIs are very large, which increases the difficulty of data storage and management [17,25,4]. Therefore, generating high-resolution images from

---

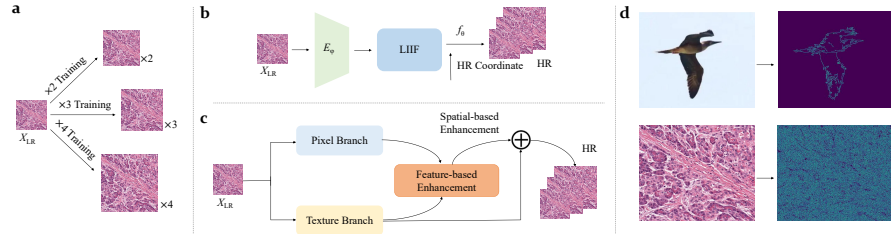[*]Linhao Qu and Minghong Duan contributed equally to this work.

Fig. 1. Motivation and architecture of the proposed ISTE. (a) All existing studies for pathology image super-resolution can only be trained and work at fixed integer scaling factors. (b) Some natural image super-resolution algorithms based on implicit neural networks [1] can perform arbitrary-scale super-resolution, but cannot properly handle WSI textures. (c) The overall architecture of ISTE, which consists of two branches and two specially-designed texture enhancement strategies. (d) Natural and pathology images and their textures extracted by using canny operator. It can be seen that, in contrast to natural images, pathology images contain richer textures of fine-grained cell morphology with special spatial arrangement.

low-resolution ones using software algorithms will largely facilitate the practical clinical analysis of pathological images [17,9].

Super-resolution (SR) technique is an effective way to solve this problem [21,27,2,22,10,26,20,19,28]. In the field of pathological image analysis, several studies [16,7,9] apply convolutional neural networks to perform SR. As shown in Fig. 1 (a), although these methods achieve good performance, they can only be trained and tested at a specific integer scale. However, pathologists usually need to continuously zoom in and out at different magnifications to perform diagnosis, so an arbitrary-scale super-resolution method is preferable. Unfortunately, to the best of our knowledge, there are currently no models that can achieve arbitrary-scale SR in the pathology field. Recently, inspired by implicit neural networks [15], some studies [1,8] have pioneered the arbitrary-scale SR for natural images. As shown in Fig. 1 (b), although these studies can be directly applied to pathology image SR, they are not effective in handling the special textures in WSIs, which is crucial in SR for pathology images. As shown in Fig. 1 (d), unlike natural images, pathology images contain richer fine-grained cell morphology textures with special spatial arrangements.

To address this challenge, an efficient dual-branch framework based on **I**mplicit **S**elf-**T**exture **E**nhancement (called ISTE) is proposed in this paper for arbitrary-scale SR of pathology images. Fig. 1 (c) briefly illustrates the overall architecture of ISTE. Specifically, ISTE contains a pixel learning branch and a texture learning branch, both of which are based on implicit neural networks [1], thus enabling the magnification of images of arbitrary scales. In the pixel learning branch, we propose the Local Feature Interactor module to obtain richer pixel features and in the texture learning branch, we propose the Texture Learner module to enhance the network's learning of texture information. After that, we design two texture enhancement strategies, namely the feature-based texture enhancement
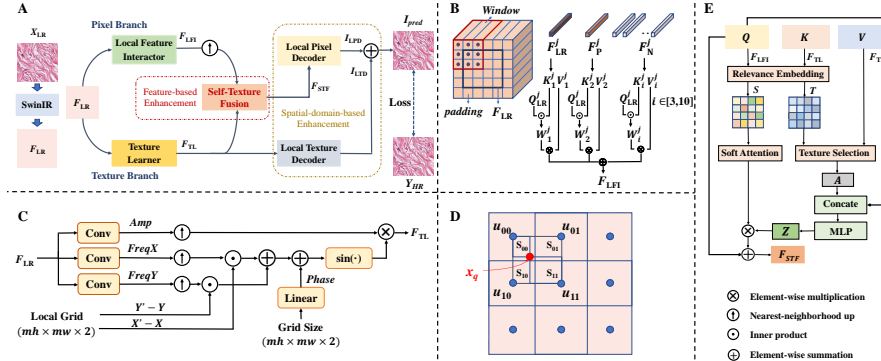
Fig. 2. Detailed architecture of our ISTE (A) and its key components. B Local Feature Interactor, C Texture Learner, D Coordinate Diagram of F_{STF} and F_{TL} for Local Pixel Decoder and Local Texture Decoder. E Self-Texture Fusion Module.

and the spatial domain-based texture enhancement, to further improve the textures of the output images. Extensive experiments on two public datasets have shown that ISTE provides better performance than existing fixed-magnification and arbitrary-magnification algorithms at multiple scales. To the best of our knowledge, this is the first work to achieve arbitrary-scale super-resolution in the field of pathology images.

2   Method

2.1   Framework Overview

Fig. 2 A shows the detailed architecture of our proposed ISTE. SwinIR [13,11] without upsampling layers is first used to extract features from the input low-resolution image X_{LR} and then the extracted feature map F_{LR} is input into the pixel branch and the texture branch, respectively. Both branches are based on implicit neural networks [1], thus enabling the magnification of arbitrary-scale images. In the pixel learning branch, the Local Feature Interactor (LFI) module is used to enhance the network's perception and interaction of local pixel features and obtain a richer pixel feature F_{LFI}. In the texture learning branch, the Texture Learner (TL) module is used to enhance the network's learning of texture information and extract the texture feature F_{TL}. After that, we utilize a two-stage texture enhancement strategy to process the output features from the two branches, where the first stage is feature-based texture enhancement and the second stage is spatial domain-based texture enhancement. Considering that pathology images contain many similar cell morphology and periodic texture patterns, we design the Self-Texture Fusion (STF) module and obtain F_{STF} to accomplish feature-based texture enhancement. After that, we obtain the output high-resolution image through spatial-domain-based texture enhancement.

Specifically, we decode the enhanced feature F_{STF} through the Local Pixel Decoder to obtain the spatial image I_{LPD}. At the same time, we use Local Texture Decoder to decode the texture feature F_{TL} to spatial texture I_{LTD}. Finally, I_{LTD} and I_{LPD} are added up through element-wise summation to obtain the output high-resolution image I_{pred}. Then, we use L1 loss to calculate the loss between it and the ground truth image. The LFI, TL and STF modules in our ISTE framework are presented in Sections 2.2, 2.3 and 2.4, respectively. The Local Pixel Decoder and Local Texture Decoder are introduced in Section 2.5.

2.2 Local Feature Interactor

As shown in Fig. 2 B, the LFI module first assigns a window of size 3×3 to each vector of the feature map F_{LR} of size $h \times w \times 64$, and we denote each vector of F_{LR} as F_{LR}^j ($j = 1, 2, ..., h \times w$). Eight neighboring vectors in the window around F_{LR}^j form a set $F_N^j = \{F_{N_i}^j | i = 3, 4, ..., 10\}$, and the pooling vector of the window is denoted as F_P^j. The feature map F_{LFI} output by the LFI module is calculated through self-attention so that each point on the feature map incorporates local features while paying more attention to itself. We denote each vector of F_{LFI} as F_{LFI}^j ($j = 1, 2, ..., h \times w$), and it is calculated through Equation 1.

$$F_{LFI}^j = \sum_{i=1}^{10} \frac{\exp\left(\left(Q_{LR}^j\right)^T K_i^j\right)}{\sqrt{d} \sum_{i=1}^{10} \exp\left(\left(Q_{LR}^j\right)^T K_i^j\right)} V_i^j,$$

(1)

where Q_{LR}^j is the Query mapped linearly from F_{LR}^j, K_1^j is the Key mapped linearly from F_{LR}^j, V_1^j is the Value mapped linearly from F_{LR}^j, K_2^j is the Key mapped linearly from F_P^j, V_2^j is the Value mapped linearly from F_P^j, $\{K_i^j | i = 3, 4, ..., 10\}$ is the Key mapped linearly from F_N^j, $\{V_i^j | i = 3, 4, ..., 10\}$ is the Value mapped linearly from F_N^j, and d is the dimension of these vectors. The parameters used by each window are shared in Self Attention calculation.

2.3 Texture Learner

Inspired by LTE [8], Texture Learner (TL) is proposed for learning texture information in pathology images. We use *sine* activation to help our model represent the cell and texture that appear periodically in pathology images. Specifically, we normalize the value of 2D coordinate $(X', Y') = \{(x'_i, y'_j) | i = 1, 2, ..., mw, j = 1, 2, ..., mh\}$ in the continuous HR image domain and the value of 2D coordinate $(X, Y) = \{(x_i, y_j) | i = 1, 2, ..., mw, j = 1, 2, ..., mh\}$ nearest to (X', Y') in the continuous LR image domain between -1 and 1, and the Local Grid is defined as $(X' - X, Y' - Y)$. Since each coordinate of the HR image has a corresponding coordinate in the LR image that is closest to it, the number of both the HR and LR image coordinate is equal to $mh \times mw$, where m represents magnification. As shown in Fig. 2 C, the TL outputs three feature maps of size $h \times w \times 256$

through three 3×3 convolutional kernels, and predicts the feature vectors Amp, $FreqX$, and $FreqY$ corresponding to each coordinate of the HR image through nearest neighbor interpolation. We use an MLP and Sigmoid activation function to map $(2/mw, 2/mh)$ to a 256-dimensional feature vector $Phase$ to simulate the effect of texture fragment offset when the image scaling factor changes. The output of the FL module is calculated by Equation 2.

$$F_{TL} = Amp \otimes Sin \left(FreqX \odot \left(X^{'} - X \right) + FreqY \odot \left(Y^{'} - Y \right) + Phase \right) \quad (2)$$

where $\otimes$ denotes the element-wise multiplication and $\odot$ denotes the inner product.

2.4 Self-Texture Fusion Module

Inspired by STSRNet [14] and T2Net [5], we propose a cross attention-based Self-Texture Fusion (STF) module. As shown in Fig. 2 E, we use the features sampled by nearest-neighborhood interpolation from F_{LFI} as the Query (Q) of the cross attention module and the F_{TL} as the Key (K) and Value (V) of the cross attention module. To retrieve the texture features that are most relevant to the pixel feature F_{LFI} from F_{TL}, we first calculate the similarity matrix R of Q and K, where each element $r_{i,j}$ of R is calculated as Equation 3, where q_i is an element of Q and k_j is an element of K. Then we obtain the coordinate index matrix T with the highest similarity to q_i in K. An element in T is $t_i = \arg\max_j (r_{i,j})$, and t_i represents the position coordinates of the texture feature k_j with the highest similarity to q_i in F_{TL}. We pick the feature vector a_i with the highest similarity to each element in Q from V according to the coordinate index matrix T to obtain the retrieved texture feature A, which can be represented by $a_i = v_{t_i}$, where a_i is an element in A and v_{t_i} represents the element at the t_i-th position in V. In order to fuse the retrieved texture feature A with the pixel feature Q, we first concatenate Q with A and obtain the aggregated feature Z through the output of an MLP, that is $Z = MLP(\text{ Concat } (Q, A))$. Finally, we calculate the soft attention map S, where an element s_i in S represents the confidence of each element a_i in the retrieved texture feature A, and $s_i = \max_j (r_{i,j})$. F_{STF} is calculated as Equation 4.

$$r_{i,j} = \left\langle \frac{q_i}{\|q_i\|}, \frac{k_j}{\|k_j\|} \right\rangle, \quad (3)$$

$$F_{STF} = Q \oplus Z \otimes S \quad (4)$$

where $\langle \cdot \rangle$ denotes the inner product, $\| \cdot \|$ denotes the L2 norm, and $\oplus$ denotes the element-wise summation.

2.5 Local Pixel Decoder and Local Texture Decoder

Inspired by LIIF [1], we propose the Local Pixel Decoder (LPD) module to decode the feature F_{STF}, into the pixel RGB value I_{LPD}. We parameterize LPD

as an MLP f_θ, where θ is the network parameter. As shown in Fig. 2 (D), u denotes the coordinates of F_{LR} and x_q denotes the coordinate of F_{STF} and F_{TL}. We use u_t ($t \in 00, 01, 10, 11$) to denote the upper-left, upper-right, lower-left, and lower-right coordinates of an arbitrary point x_q, respectively, and the RGB value of x_q in the HR image LPD can be expressed by Equation 5, where $I_{LPD}(x_q)$ is the RGB value of x_q in image I_{LPD}, c contains two elements, $2/mh$ and $2/mw$, which are the pixel size of I_{LPD} and facilitate the decoding of pixel information. Similarly, we parameterize the I_{LTD} as an MLP g_φ, and the RGB values corresponding to the I_{LTD} coordinates x_q of the texture-informed image output by the spatial domain-based texture enhancement can be caluclated by Equation 6. We decode the texture features into texture information I_{LTD} by the LTD module and add it to I_{LPD} to achieve the texture enhancement, where φ is the network parameter of the MLP g_φ, S_t ($t \in 00, 01, 10, 11$) is the area of the rectangular region between x_q and u_t, and the weights are normalized by $S = \sum_{t \in \{00, 01, 10, 11\}} S_t$.

$$I_{LPD}\left(x_q\right) = \sum_{t \in \{00,01,10,11\}} \frac{s_t}{s} \cdot f_\theta\left(F_{STF}, x_q - u_t, c\right), \tag{5}$$

$$I_{LTD}\left(x_q\right) = \sum_{t \in \{00,01,10,11\}} \frac{s_t}{s} \cdot g_\varphi\left(F_{TL}\right), \tag{6}$$

3 Experiments

3.1 Datasets, Competitors, Metrics and Implementation Details

We used TMA Dataset [3,9] and TCGA lung cancer dataset for experiments. For the TMA Dataset, we randomly selected 460 WSIs (average 3850×3850 pixels each) as the training set, 57 WSIs as the validation set, and 56 WSIs as the test set. For the TCGA dataset, we selected 5 slides (average 100000×100000 pixels each) cut into 400 sub-images of 3072×3072, and randomly selected 320 as the training set, 40 as the validation set, and 40 as the test set.

We compared the performance of ISTE with SOTA SR methods in both the pathology image domain: Li et al. [9], and the natural image domain: Bicubic, EDSR [12], LIIF [1] and LTE [8], where the latter two are implicit neural network-based methods. For a fair comparison, the backbone used for LIIF and LTE is also SwinIR [11] without upsampling layers. Following these studies, our evaluation metrics include structural similarity (SSIM), peak signal-to-noise ratio (PSNR), and Frechet Inception Distance (FID).

Following LIIF [1], we used a 48×48 patch as the input for training. We first randomly sampled the magnification m in a uniform distribution $U(1, 4)$, and cropped patches with size of $48m \times 48m$ from training images in a batch. We then resized the patches to 48×48 and did a Gaussian blur to simulate degradation. For the ground truth images, we sampled 48^2 pixels from the corresponding cropped patches to form RGB-Coordinate pairs. We used PyTorch with Adam as the optimizer, setting the initial learning rate to 0.0001 and epochs to 1000.

Table 1. Performance comparison of the methods on the TMA and TCGA datasets.

Dataset	Method	In-distribution						Out-of-distribution								
		×2			×3			×4			×6			×8		
		PSNR↑	FID↓	SSIM↑	PSNR↑	FID↓	SSIM↑	PSNR↑	FID↓	SSIM↑	PSNR↑	FID↓	SSIM↑	PSNR↑	FID↓	SSIM↑
TMA	Bicubic	27.02	12.19	0.8559	24.17	39.41	0.7289	22.62	69.32	0.6387	20.94	117.22	0.5426	19.98	155.44	0.4972
	EDSR (CVPR2017)	28.79	6.97	0.8923	23.60	24.33	0.7259	23.88	49.68	0.7002	21.79	88.92	0.5909	20.65	114.05	0.5371
	LIIF (CVPR2021)	31.10	3.39	0.9427	27.95	5.45	0.8764	25.99	15.71	0.8035	23.64	50.76	0.6833	22.20	80.61	0.6037
	LTE (CVPR2022)	31.26	3.11	0.9432	28.22	5.27	0.8787	26.25	14.37	0.8093	23.75	51.78	0.6823	22.18	80.98	0.5982
	Li's (MIA2021)	29.70	6.52	0.9106	26.19	18.89	0.8357	24.15	46.23	0.7537	20.45	95.04	0.6188	18.71	137.52	0.5425
	Ours	**32.71**	**2.87**	**0.9445**	**28.77**	**4.85**	**0.8815**	**26.70**	**13.76**	**0.8142**	**23.90**	**50.76**	0.6822	**22.22**	**78.78**	0.5953
TCGA	Bicubic	28.89	15.94	0.8791	25.78	57.40	0.7348	24.00	105.76	0.6230	22.02	190.59	0.4959	20.85	257.01	0.4347
	EDSR (CVPR2017)	30.80	5.59	0.9047	27.37	46.01	0.7803	25.43	112.04	0.6776	23.23	204.64	0.5506	21.90	241.72	0.4814
	LIIF (CVPR2021)	36.25	1.53	0.9716	31.62	2.81	0.9073	28.69	19.90	0.8187	25.31	96.44	0.6564	23.55	136.12	0.5545
	LTE (CVPR2022)	36.65	1.31	0.9729	31.87	3.12	0.9094	28.95	18.61	0.8244	25.44	92.17	0.6597	23.62	125.45	0.5559
	Li's (MIA2021)	33.53	3.86	0.9472	29.74	28.56	0.8716	27.42	57.43	0.7844	24.29	116.18	0.6230	22.83	140.12	0.5334
	Ours	**38.28**	**1.22**	**0.9748**	**32.46**	2.92	**0.9111**	**29.33**	**17.42**	**0.8287**	**25.64**	**88.00**	**0.6617**	**23.74**	119.98	**0.5578**

3.2 Experimental Results

We compared our ISTE with competitors at five magnifications of ×2, ×3, ×4, ×6, and ×8. Table 1 show the results on the TMA and TCGA datasets. As can be seen, ISTE achieves the highest performance in almost all metrics at all magnifications. It is worth noting that the existing SOTA methods in the field of pathology image SR, Li's method [9] cannot achieve arbitrary-scale magnification, so they need to be retrained at each magnification, whereas our method needs only a one-time training. Even so, our method outperforms Li's method [9] with a large margin. On the other hand, compared to the other two implicit neural network-based methods LIIF [1] and LTE [8] in the field of natural images, our method also shows superior performance in most of the metrics.

Fig. 3 shows the visualization of the super-resolution results and the error maps at ×4 magnification. It can be seen that ISTE recovers textures better and ISTE's results are more similar to the ground truth images. Fig. 4 A shows the non-integral magnification of LIIF and our ISTE. It can be seen that ISTE achieves arbitrary magnification with clear cell structure and texture features. In larger magnification, ISTE outperforms LIIF in terms of visual effect. More visual comparisons with error maps of different methods on the TMA and TCGA datasets are shown in Fig. 5. More visual results of our method at arbitary magnifications on the TMA and TCGA datasets are shown in Fig. 6.

4 Ablation Study

We designed four variants of the network for ablation experiments on the TCGA dataset, and Table 2 shows the results. The main variants are as follows: **(2) w/o LFI**, remove the Local Feature Interactor module from our model; **(3) w/o STF**, remove the Self-Texture Fusion module from our model, and add the pixel information decoded by the Pixel Feature directly through the Local Pixel Decoder to the output of the Local-Texture Decoder module; **(4) w/o LTD**, remove the Local-Texture Decoder module from our model, and the features are directly decoded into pixel information as output by Local Pixel Decoder after the interaction between Pixel Feature and Texture Feature. The results
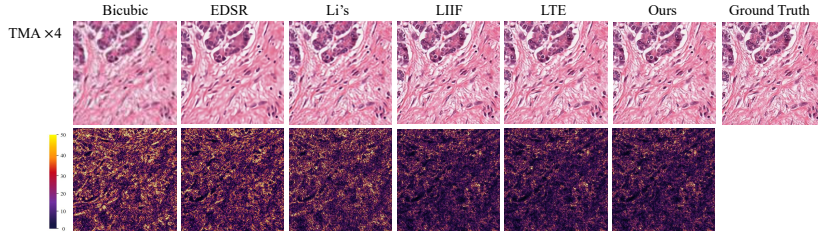
Fig. 3. Visual comparison with error maps of different methods on the two datasets. The error maps represent the absolute values of the error between the outputs and the ground truth images, with brighter colors representing larger errors.

demonstrate the efficiency of each component of ISTE. We also visualized the effect of texture transfer of STF. Fig. 4 B (b4) indicates the texture transfer during one training iteration, where the blue arrows represent the direction of texture transfer. This demonstrates that our STF module does play a role in texture transfer. Further, we visualized the pixels decoded by LPD and the textures decoded by LTD. As shown in Fig. 4 B (b1-b3), the pixel information decoded with LPD alone is relatively smooth and lacks high-frequency texture details, while the texture information decoded by LTD shows clear contours and textures of cells. This further illustrates the importance of spatial domain-based texture enhancement with LTD. More visual results of the ablation study on the TCGA dataset are shown in Fig. 7.
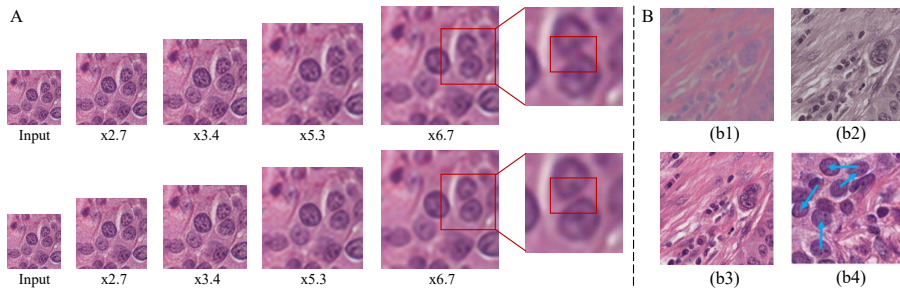

Fig. 4. A. Non-integral magnification results of LIIF (upper row) and our ISTE (lower row). As shown in the red box, at the magnification of ×6.7, two cells are connected due to blurring in the image generated by LIIF, while they are still separated in the image generated by ISTE. B. (b1). Pixels decoded by LPD (b2). Textures decoded by LTD (b3). Ground truth image (b4). Visualization of texture similarity retrieval for the STF module, where the starting position of the blue arrow indicates the position of the retrieved texture feature F_{TL} in the STF module, and the position pointed by the arrow is the position of the pixel feature that needs to be fused with the retrieved texture feature F_{TL} enhancement.
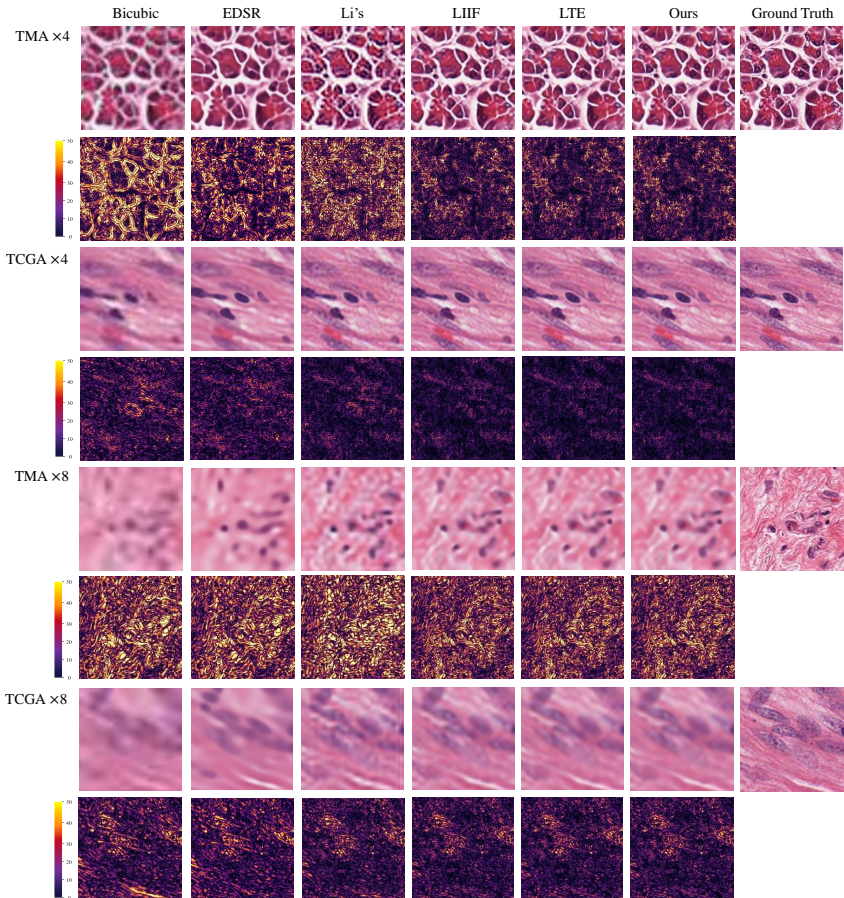
Fig. 5. More visual comparisons with error maps of different methods on the TMA and TCGA datasets at 4× and 8× magnifications. The error maps represent the absolute values of the error between the outputs and the ground truth images, with brighter colors representing larger errors.
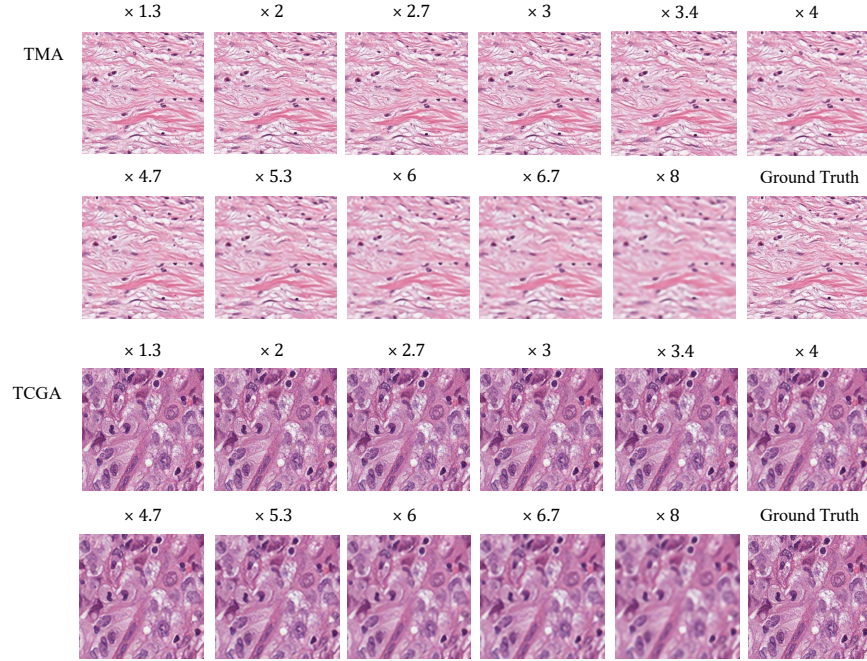
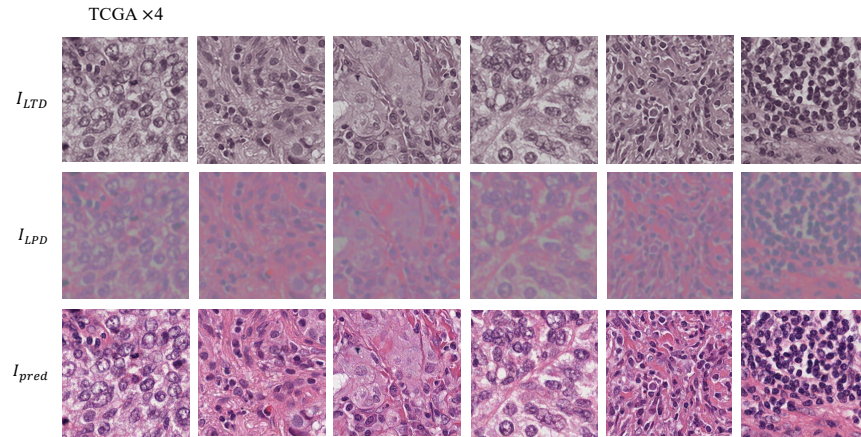**Fig. 6.** More visual results of our method at arbitary magnifications on the TMA and TCGA datasets.

Fig. 7. More visual results of the ablation study on the TCGA dataset. The first row: pixels decoded by LPD. The second row: textures decoded by LTD. The third row: final predictions.

Table 2. Results of ablation studies on the TCGA dataset.

	×2			×3			×4			×6			×8		
	PSNR↑	FID↓	SSIM↑	PSNR↑	FID↓	SSIM↑	PSNR↑	FID↓	SSIM↑	PSNR↑	FID↓	SSIM↑	PSNR↑	FID↓	SSIM↑
Ours	**38.28**	**1.22**	**0.9748**	**32.46**	2.92	**0.9111**	**29.33**	17.42	**0.8287**	**25.64**	**88.00**	0.6617	**23.74**	119.98	0.5578
w/o LFI	36.69	1.29	0.9727	31.90	3.06	0.9095	28.96	18.29	0.8250	25.50	89.36	0.6630	23.67	120.76	0.5591
w/o STF	36.82	1.25	0.9737	31.94	2.98	0.9103	29.05	**17.22**	0.8274	25.57	88.47	**0.6658**	23.74	121.80	**0.5619**
w/o LTD	36.76	1.29	0.9737	31.90	3.04	0.9099	29.02	17.62	0.8264	25.52	87.54	0.6639	23.69	**119.12**	0.5600

5 Conclusion

In this paper, we propose a novel dual-branch framework to achieve arbitrary-scale pathology image super-resolution for the first time. The proposed method outperforms SOTA natural and pathology image super-resolution methods in extensive experiments.

References

1. Chen, Y., Liu, S., Wang, X.: Learning continuous image representation with local implicit image function. In: Proceedings of the IEEE/CVF Conference on Computer Vision and Pattern Recognition. pp. 8628–8638 (2021)
2. Dong, S., Hangel, G., Bogner, W., Widhalm, G., Rössler, K., Trattnig, S., You, C., de Graaf, R., Onofrey, J.A., Duncan, J.S.: Multi-scale super-resolution magnetic resonance spectroscopic imaging with adjustable sharpness. In: Medical Image Computing and Computer Assisted Intervention. pp. 410–420. Springer (2022)
3. Drifka, C.R., Loeffler, A.G., Mathewson, K., Keikhosravi, A., Eickhoff, J.C., Liu, Y., Weber, S.M., Kao, W.J., Eliceiri, K.W.: Highly aligned stromal collagen is a negative prognostic factor following pancreatic ductal adenocarcinoma resection. Oncotarget **7**(46), 76197 (2016)
4. Feng, C.M., Fu, H., Yuan, S., Xu, Y.: Multi-contrast mri super-resolution via a multi-stage integration network. In: Medical Image Computing and Computer Assisted Intervention. pp. 140–149. Springer (2021)
5. Feng, C.M., Yan, Y., Fu, H., Chen, L., Xu, Y.: Task transformer network for joint mri reconstruction and super-resolution. In: Medical Image Computing and Computer Assisted Intervention. pp. 307–317. Springer (2021)
6. Gilbertson, J.R., Ho, J., Anthony, L., Jukic, D.M., Yagi, Y., Parwani, A.V.: Primary histologic diagnosis using automated whole slide imaging: a validation study. BMC Clinical Pathology **6**, 1–19 (2006)
7. Juhong, A., Li, B., Yao, C.Y., Yang, C.W., Agnew, D.W., Lei, Y.L., Huang, X., Piyawattanametha, W., Qiu, Z.: Super-resolution and segmentation deep learning for breast cancer histopathology image analysis. Biomedical Optics Express **14**(1), 18–36 (2023)
8. Lee, J., Jin, K.H.: Local texture estimator for implicit representation function. In: Proceedings of the IEEE/CVF Conference on Computer Vision and Pattern Recognition. pp. 1929–1938 (2022)
9. Li, B., Keikhosravi, A., Loeffler, A.G., Eliceiri, K.W.: Single image super-resolution for whole slide image using convolutional neural networks and self-supervised color normalization. Medical Image Analysis **68**, 101938 (2021)
10. Li, G., Lyu, J., Wang, C., Dou, Q., Qin, J.: Wavtrans: Synergizing wavelet and cross-attention transformer for multi-contrast mri super-resolution. In: Medical Image Computing and Computer Assisted Intervention. pp. 463–473. Springer (2022)

11. Liang, J., Cao, J., Sun, G., Zhang, K., Van Gool, L., Timofte, R.: Swinir: Image restoration using swin transformer. In: Proceedings of the IEEE/CVF International Conference on Computer Vision. pp. 1833–1844 (2021)
12. Lim, B., Son, S., Kim, H., Nah, S., Mu Lee, K.: Enhanced deep residual networks for single image super-resolution. In: Proceedings of the IEEE Conference on Computer Vision and Pattern Recognition Workshops. pp. 136–144 (2017)
13. Liu, Z., Lin, Y., Cao, Y., Hu, H., Wei, Y., Zhang, Z., Lin, S., Guo, B.: Swin transformer: Hierarchical vision transformer using shifted windows. In: Proceedings of the IEEE/CVF International Conference on Computer Vision. pp. 10012–10022 (2021)
14. Ma, J., Liu, S., Cheng, S., Chen, R., Liu, X., Chen, L., Zeng, S.: Stsrnet: Self-texture transfer super-resolution and refocusing network. IEEE Transactions on Medical Imaging **41**(2), 383–393 (2021)
15. Mildenhall, B., Srinivasan, P.P., Tancik, M., Barron, J.T., Ramamoorthi, R., Ng, R.: Nerf: Representing scenes as neural radiance fields for view synthesis. Communications of the ACM **65**(1), 99–106 (2021)
16. Mukherjee, L., Keikhosravi, A., Bui, D., Eliceiri, K.W.: Convolutional neural networks for whole slide image superresolution. Biomedical Optics Express **9**(11), 5368–5386 (2018)
17. Pantanowitz, L., Hornish, M., Goulart, R.A., et al.: The impact of digital imaging in the field of cytopathology. Cytojournal **6**(6), 4103 (2009)
18. Pantanowitz, L., Valenstein, P.N., Evans, A.J., Kaplan, K.J., Pfeifer, J.D., Wilbur, D.C., Collins, L.C., Colgan, T.J.: Review of the current state of whole slide imaging in pathology. Journal of Pathology Informatics **2**(1), 36 (2011)
19. Sood, R.R., Shao, W., Kunder, C., Teslovich, N.C., Wang, J.B., Soerensen, S.J., Madhuripan, N., Jawahar, A., Brooks, J.D., Ghanouni, P., et al.: 3d registration of pre-surgical prostate mri and histopathology images via super-resolution volume reconstruction. Medical Image Analysis **69**, 101957 (2021)
20. Sui, Y., Afacan, O., Gholipour, A., Warfield, S.K.: Mri super-resolution through generative degradation learning. In: Medical Image Computing and Computer Assisted Intervention. pp. 430–440. Springer (2021)
21. Tsang, C.S., Mok, T.C., Chung, A.C.: Joint denoising and super-resolution for fluorescence microscopy using weakly-supervised deep learning. In: Medical Optical Imaging and Virtual Microscopy Image Analysis: First International Workshop, MOVI 2022, Held in Conjunction with MICCAI 2022, Singapore, September 18, 2022, Proceedings. pp. 32–41. Springer (2022)
22. Wang, J., Wang, R., Tao, R., Zheng, G.: Uassr: Unsupervised arbitrary scale super-resolution reconstruction of single anisotropic 3d images via disentangled representation learning. In: Medical Image Computing and Computer Assisted Intervention. pp. 453–462. Springer (2022)
23. Weinstein, R.S., Descour, M.R., Liang, C., Barker, G., Scott, K.M., Richter, L., Krupinski, E.A., Bhattacharyya, A.K., Davis, J.R., Graham, A.R., et al.: An array microscope for ultrarapid virtual slide processing and telepathology. design, fabrication, and validation study. Human Pathology **35**(11), 1303–1314 (2004)
24. Wilbur, D.C.: Digital cytology: current state of the art and prospects for the future. Acta Cytologica **55**(3), 227–238 (2011)
25. Wilbur, D.C., Madi, K., Colvin, R.B., Duncan, L.M., Faquin, W.C., Ferry, J.A., Frosch, M.P., Houser, S.L., Kradin, R.L., Lauwers, G.Y., et al.: Whole-slide imaging digital pathology as a platform for teleconsultation: a pilot study using paired subspecialist correlations. Archives of Pathology & Laboratory Medicine **133**(12), 1949–1953 (2009)

26. Wu, Q., Li, Y., Xu, L., Feng, R., Wei, H., Yang, Q., Yu, B., Liu, X., Yu, J., Zhang, Y.: Irem: high-resolution magnetic resonance image reconstruction via implicit neural representation. In: Medical Image Computing and Computer Assisted Intervention. pp. 65–74. Springer (2021)

27. Yu, P., Zhang, H., Kang, H., Tang, W., Arnold, C.W., Zhang, R.: Rplhr-ct dataset and transformer baseline for volumetric super-resolution from ct scans. In: Medical Image Computing and Computer Assisted Intervention. pp. 344–353. Springer (2022)

28. Zeng, R., Lv, J., Wang, H., Zhou, L., Barnett, M., Calamante, F., Wang, C.: Fod-net: A deep learning method for fiber orientation distribution angular super resolution. Medical Image Analysis **79**, 102431 (2022)